

A mixed radial, angular, three-body distribution function as a tool for local structure characterization: Application to single-component structures

Sergey V. Sukhomlinov^{1,*} and Martin H. Müser¹

¹*Dept. of Materials Science and Engineering, Universität des Saarlandes, Saarbrücken, Germany*

A mixed radial, angular three-body distribution function $g_3(r_{BC}, \theta_{ABC})$ is introduced, which allows the local atomic order to be more easily characterized in a single graph than with conventional correlation functions. It can be defined to be proportional to the probability of finding an atom C at a distance r_{BC} from atom B while making an angle θ_{ABC} with atoms A and B, under the condition that atom A is a nearest neighbor of B. As such, our correlation function contains, for example, the likelihood of angles formed between nearest and next-nearest-neighbor bonds. To demonstrate its use and usefulness, a visual library for many one-component crystals is produced first and then employed to characterize the local order in a diverse body of elemental condensed-matter systems. Case studies include the analysis of a grain boundary, several liquids (argon, copper and antimony), polyamorphism in crystalline and amorphous silicon including that obtained in a tribological interface.

I. INTRODUCTION

Computer simulations of condensed matter systems are often run with the goal to ascertain the degree with which the local structure of systems lacking long-range order resembles that of crystalline reference phases. Examples relate to the interpretation of liquid-liquid transitions in terms of a competition between different local structures [1–6], or, the attempt to explain the contrast of electrical and mechanical properties between crystalline and amorphous materials in phase-change materials with a change of local order that occurs at the amorphous to crystalline transition [7, 8].

The most frequently studied observable allowing some conclusions on local structure to be drawn is the radial distribution function (RDF) $g(r)$. It plays an important role also because of its direct connection to x-ray diffraction patterns [9]. However, it is usually very difficult to distinguish between different local orders in disordered systems using the RDF alone, amongst other reasons, because its second peak may or may not include the third neighbor shell in addition to the second. Thus, while the coordination number of the sought-after reference crystal can be usually estimated from the first peak of the RDF, in particular when performing a skewed Gaussian analysis of it [10], a similar, even rough estimate for the number of atoms in the second coordination shell cannot be deduced from the analysis of the RDF's second peak. Finally, it is generally not possible to ascertain the main reason—potential candidates being thermal fluctuations, positional disorder, lattice defects, or collective displacive modes—for why the first peak in the RDF is broadened or skewed from the RDF itself.

The natural extension of the RDF is the triplet correlation function (TCF) $g(r_{ij}, r_{ik}, r_{jk})$, which implicitly includes information on bond angles, since a triangle is fully defined by the lengths of its three edge lengths.

While the analysis of the full TCF can certainly be very useful, for example, to quantify many-body effects in potential energy surfaces [11], it defies a general, graphical representation in a single figure, because visualizable correlation functions can depend at most on two independent variables. For this reason, several projections of the TCF have been considered. These include dropping one of the three pair distances, leading to the three-body distribution function $g(r_{ij}, r_{ik})$ [12, 13], which we call TCF1, or, restraining two of them to be close to each other [11, 14, 15] leading to $g(r_{ij}, r_{ik} \approx r_{ij}, r_{jk})$, which we call TCF2. Both reduced TCFs certainly have their own merit, e.g., TCF2 allows the distribution of isosceles triangles to be determined, which has proven useful in the characterization of tetrahedral liquids such as water [16–21] and silicon [22, 23]. However, information on bond angles is absent in TCF1, while it is not clear that the information on bond angles contained in TCF2 adds to direct measurements of bond-angle distribution functions.

Information on bond angles can be obtained from the bond-angle distribution function and bond-orientational order parameters deduced from it [24]. However, these are only sensitive to the nearest-neighbor shell. Even worse, in disordered systems, they are only meaningfully defined when augmented with non-trivial, Voronoi-analysis based weighting functions [25]. An angular-radial distribution function (ARDF) [26–28] has been introduced, which, like our distribution function introduced further below, depends on one distance and one angle. However, our distribution function is a three-body correlation function, while the ARDF is a six-point correlation function. Its definition requires knowledge of two molecular centers of mass, from which the intermolecular separation can be defined, and, in addition, two (end) points per molecules for the calculation of the molecular directors and the angle between them.

Another powerful, frequently used and very effective method for the characterization of local, structural motifs, is the Voronoi tessellation. Since it is a discrete anal-

* sergey.sukhomlinov@uni-saarland.de

ysis tool, for which results can be susceptible to small (temporal) fluctuations, it provides useful complementary information to correlation functions, but does not allow the information contained in them to be reconstructed. Moreover, Voronoi tessellations only senses the local order. Thus, while all mentioned characterization methods are certainly useful, it would be beneficial to have an additional analysis tool in place that (a) is sensitive to bond angles, (b) can see past the nearest-neighbor shell, (c) requires no or very little biased input by the simulator, and (d) allows for simple visualization.

In this work, we propose that a mixed radial, angular three-body distribution function satisfies the just-mentioned demands. The arguably most significant added value of the proposed distribution function, compared to the other mentioned distribution functions, is that it allows angles between nearest-neighbor bonds and “bonds” between the central and a more distant atom to be readily deduced. We demonstrate the use of our correlation function as well its usefulness for a broad class of elementary condensed-matter systems ranging from small perturbation of perfect crystalline order to highly disordered, out-of-thermal-equilibrium structures. Although work on binary and ternary systems is in mature progress, it is not presented here to reduce the risk of making this publication unbearably extensive.

The remainder of this paper is organized as follows. We define the distribution function in Sec. II, where we also construct a visual reference library for monoatomic crystals. A variety of applications are covered in Sec. III including monoatomic liquids, grain boundaries and tribological interfaces, the purpose being predominantly pedagogical in nature. Conclusions are drawn and an outlook is given in Sec. IV.

II. DEFINITION, METHODS, AND VISUAL REFERENCE LIBRARY

A. Definition

Although applications in this work focus on elementary systems, we provide the general definition for the mixed radial, angular distribution function $g_3(r_{BC}, \theta_{ABC})$ that also holds for many-component systems. A graphical representation of the terms entering the definition of g_3 is provided in Fig. 1. Our correlation function is defined to be proportional to the probability of finding a C atom at a distance r_{BC} from a B atom when the angles between \mathbf{r}_{BC} and \mathbf{r}_{BA} take the value θ_{ABC} under the condition that the A atom and the B atom are nearest neighbors. Here, \mathbf{r}_{BC} and \mathbf{r}_{BA} are the vectors pointing from the B atom to the C atom and from the B atom to the A atom, respectively. The distribution function is normalized such that it would equal unity if the considered system were an ideal gas at the given density. We note that the proposed correlation function contains similar information as a projection of the TCF

to $g(r_{AB} \approx d_{AB}, r_{BC}, r_{AC})$, i.e., to a cut through the TCF on the plane, where type A and type B atoms are nearest neighbors. The probably most important advantage of our projection of $g(r_{ij}, r_{ik}, r_{jk})$ compared to other projections is that it contains information on the distribution of angles between a nearest-neighbor bond and a vector connecting a central atom with a more distant atom.

The computation of g_3 requires the specification of two seemingly *ad-hoc* parameters, specifically, d_{AB} and how large of a deviation from d_{AB} is allowed for r_{AB} to qualify as a nearest-neighbor distance. Before discussing how to select these two parameters, we note that we found their precise definition not to matter in the overwhelming number of applications as long as choices are reasonable.

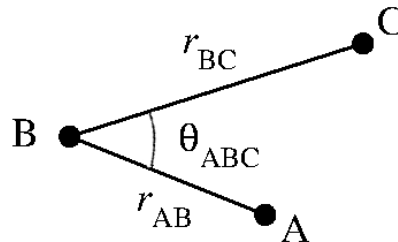


FIG. 1. Graphical representation of the terms entering the definition of the mixed radial, angular distribution function $g_3(r_{BC}, \theta_{ABC})$. Atoms of type A and B are requested to be nearest neighbors, or, to be separated by a distance close to their mean bond lengths.

A characteristic bond length $d_{AB}(r)$ can be defined as the most likely nearest-neighbor distance between atom types A and B, which is the location of the first maximum of $r^2 g_{AB}(r)$, where $g_{AB}(r)$ is the AB radial distribution function. A slightly more accurate mean bond length can be obtained through a skewed normal distribution (SND) analysis of the first peak of $r^2 g_{AB}(r)$ [10]. For the margin, one might restrict r_{AB} , for example, to values less or equal $d_{AB} + \sigma_{AB}$, where σ_{AB} reflects a well-chosen deviation, e.g., the half width of the nearest-neighbor peak in $r^2 g_{AB}(r)$, which can again be deduced from a Gaussian or SND-fit to $r^2 g_{AB}(r)$. More elaborate partitioning schemes are possible. For example, first and second peak in $r^2 g(r)$ could be subjected to an SND analysis and a relative probability or weight be deduced for values of r lying between the first and second maximum of $g(r)$ which states the probability of a given value of r to belong to the first or to the second peak. A last, but computationally demanding possibility to judge if A and B are neighbors can be achieved through a Voronoi analysis, which would satisfy the definition of g_3 in the abstract. This latter approach could certainly be further refined with weighting schemes as those pursued in the construction of orientational bond-order parameters [25]. However, the need to do so is reduced, because information on angles and distances is retained in our correlation function.

While a unique definition of g_3 for which atoms qualify

as neighbors might be desirable, we believe that the used definition is best selected depending on the system of interest and the number of configurations that can be sampled over. In particular, when a system has short and long bonds, e.g., when a weak Peierls deformation or Jahn-Teller distortion is present, simulators might have to decide whether or not the long bonds should be treated as nearest-neighbor bonds.

Reasonable values of d_{AB} should be frequently known before the simulation is started so that $g_3(r_{BC}, \theta_{ABC})$ can be directly measured on the fly. Alternatively, the two-body RDF $g_{AB}(r)$ could be measured first, allowing an unbiased estimate of d_{AB} , and $g_3(r_{BC}, \theta_{ABC})$ could be determined in post-analysis as discussed above, or, on the fly, after d_{AB} has been determined to a desired accuracy.

1. A note on nomenclature and plotting

In the following text, we will “overload” the symbol g representing distribution functions and assume that the reader identifies the correct interpretation by analysis of arguments and context. For example, $g(r)$, $g_2(r)$, or $g_{AB}(r)$ are all meant to refer to the regular two-body distribution function. In contrast, $g(r, \theta)$ or $g_3(r, \theta)$ is meant to refer to our mixed radial, angular distribution function, while $g_3(r, r)$ would refer to the three-body distribution function introduced in Ref. 12. In a non-elemental system, $g_{ABC}(r, \theta)$ or $g(r_{BC}, \theta_{AC})$ would both indicate the same three-body function. If g_3 is mentioned without further explanation, we mean to refer by default to the mixed radial, angular distribution function, introduced in this work.

In this section, we also wish to provide our rationale for the choice of y -axis in figures showing g_3 . We preferred the use of $\cos \theta$ over θ , because the *a-priori* probability density of finding another neighbor at a given value of $\cos \theta$ is constant, while the one for finding another neighbor under an angle θ changes proportionally with $\sin \theta$. At the same time, we chose to let the y -axis go from negative (-1) to positive (+1) numbers as this makes the values of θ go from 0 to π . Note however, that peaks in g_3 at $\cos \theta = \pm 1$ may not always be immediately visible.

Finally, we note that the term “max” in the color bar of g_3 graphs indicates any intensity exceeding the value being assigned the label “max”. However, the color coding between 0 and “max” is linear.

B. Numerical methods

For the specific examples introduced in the construction of the visual reference library, we ran brief simulations that were based on either DFT or simple model potentials. The purpose of running these simulations was not to produce highly accurate, numerical results but rather to provide a reference in which the ideal crystalline

peaks were broadened in a way that should be characteristic for the given system at special points in the phase diagram or simply at ambient conditions. Thus, the DFT methods and classical interaction potentials used for the applications are not necessarily the best on the market for the modeling of a given system either, although an attempt was made to pursue reasonable descriptions. As such, conclusions on liquid argon are rather conclusions on Lennard-Jones melt while simulations of copper relate to a general system with Gupta potential interactions even if our judgment of the Gupta potential [29] w.r.t. its ability to model copper is certainly quite positive [30]. Thus, the main emphasis of this work is to demonstrate how to obtain structural information from the g_3 distribution function.

Roughly one half of our elemental compounds was described with DFT. The calculations were based on the PBE exchange-correlation functional [31], and the Gaussian Plane Waves (GPW) method [32] as implemented in CP2K [33]. We used Gaussian basis sets of double- ζ [34] quality in a combination with Goedecker-Teter-Hutter (GTH) pseudopotentials [35, 36], and sampled only Gamma point as the systems were reasonable large in size. Energy cutoffs, particle numbers, and box shapes were chosen to be as follows: (b) Mg (400 Ry, 36, $9.6 \text{ \AA} \times 9.6 \text{ \AA} \times 10.4 \text{ \AA}$, hexagonal box with $\gamma=120^\circ$), (c) Na (400 Ry, 54, $12.9 \text{ \AA} \times 12.9 \text{ \AA} \times 12.9 \text{ \AA}$, cubic box), (g) In (400 Ry, 128, $13.0 \text{ \AA} \times 13.0 \text{ \AA} \times 19.8 \text{ \AA}$, orthorhombic box), and (h) Sb (400 Ry, 192, $16.9 \text{ \AA} \times 16.9 \text{ \AA} \times 21.1 \text{ \AA}$, hexagonal box with $\gamma=120^\circ$).

The remaining structures were simulated with classical force fields, specifically: (a) Cu (Gupta potential [29], as parametrized by Jalkanen *et. al.* [30]), (d) NaCl, used to simulate a pseudo-SC g_3 (embedded-ion model by Zhou *et. al.* [37]), (e) Si diamond (Tersoff potential [38], parametrized by Kumagai [39]), and (f) C graphite (Tersoff potential [38]). In the results section, we also provide results on Al, which was modeled with an EAM potential [40].

All simulations were run either using CP2K [33] or LAMMPS [41] or were courtesy of Thomas Reichenbach [42]. All analysis was conducted as post processing of the configuration files. In all runs of classical MD, Langevin [43] thermostats acted on atoms, whereas CSVR thermostats [44] were chosen for all *ab initio* simulations. In all cases, Nose-Hoover chains [45] were used as barostats whenever pressure was set constant.

C. Visual reference library for selected elemental crystals

The number of elemental crystalline structures is rather long. This is why we restrict our attention primarily to those monoatomic structures whose elementary cell is fully defined by a single parameter, i.e., the volume of the unit cell. These are (underlined chemical symbols denoting those elements serving as specific examples in

the following):

- (a) face-centered cubic (fcc), e.g., Al, Ca, Ni, Cu, Sr, Rh, Pd, Ag, Pt, Au, and noble gases except He. Allowed angles are 60° , 90° , 120° and 180° . Allowed secondary angles are 45° , 90° , 135° and 180° .
- (b) hexagonal close packed (hcp), e.g., He, Be, Mg, Co, and Zn. Allowed bond angles 60° , 90° , 120° and 180° . Allowed secondary angles are 45° , 90° , 135° and 180° .
- (c) body-centered cubic (bcc), e.g., Cr, Mn, Fe, Mo, W, and alkali metals including Na. Allowed bond angles satisfy $\cos\theta = \pm 1/3$ and $\cos\theta = -1$. Allowed secondary angles satisfy $\cos\theta = \pm 1/\sqrt{3}$.
- (d) simple cubic (sc), e.g., Po. Allowed bond angles 90° and 180° . Allowed secondary angles are 45° , 90° and 135° .
- (e) diamond cubic (dc), e.g., Si and Ge. Allowed bond angle satisfies $\cos\theta = -1/3$. Allowed secondary angles satisfy $\cos\theta = \pm\sqrt{6}/3$ and $\cos\theta = 0$.

In this list, the term secondary angles refers to angles between a vector pointing from a central atom to a nearest neighbor and another vector pointing from a central atom to a next-nearest neighbor, assuming perfect crystalline order. From the list above we were not able to stabilize a simple cubic structure of As at pressures of up to 40 GPa, which was reported in the literature to be the high-pressure phase at $p \approx 25$ GPa [46]. For this reason we produced the mixed radial, angular three-body distribution function for a simple cubic crystal by considering NaCl structure while treating all atoms in the post-analysis as being of the same type, even if only the (classical) $T = 0$ configuration would be strictly simple cubic. Broadening of the peaks differ between Na or Cl being the atom B in the general $g_3(r_{BC}, \theta_{ABC})$ expression.

We also include two selected single-component structures in which two parameters are needed to construct the unit cell, in addition to hcp, which requires the precise c/a ratio for non-ideal hcp. These are:

- (f) hexagonal (hex), as in graphite. Allowed bond angles 120° . Allowed secondary angles are 30° , 90° and 150° .
- (g) face-centered tetragonal (fct), specifically A6, as in In. Allowed bond angles and allowed secondary angles are close to but not identical to those of hcp.

Lastly, one structure is included, in which the Wyckoff position of at least one atom needs to be specified, in order to define the crystal. This structure is

- (h) rhombohedral, specifically hexagonal A7, as an example for a solid with a weak Peierls deformation, e.g., As, Sb, Bi. Allowed primary bond angles are

close to 90° , and 180° . Allowed secondary angles are 45° , 90° , and 135° , again within a few arc degrees.

A continuous transformation between two crystalline structures is also explored, namely the Bain's path connecting fcc and bcc. It is discussed in a separate section II C 1.

In the following, we will discuss some selected pairs of g_3 patterns in Fig. 2 to address questions like: if a sample had crystallites — or local order in a glass or liquid — of a given local symmetry, how could we distinguish it from another one?

Two structures that can be difficult to discriminate from each other by analyzing the regular short-range, two-body RDF are fcc and hcp, in particular because they have the same number of nearest and next-nearest neighbors while having identical ratios of nearest and next-nearest neighbor distances. However, when using $g_3(r, \theta)$, fcc and hcp are readily distinguishable at small scales, because the fcc structure has only three peaks centered at the nearest-neighbor distance, while hcp has five, which reduce to four as the ideal c/a ratio of $\sqrt{8/3}$ is approached.

While hcp has more peaks than fcc, bcc has fewer. In particular, the $\theta = 90^\circ$ peak is missing, which makes it easy to distinguish bcc from fcc in a g_3 analysis. However, it is worth keeping in mind that bcc and fcc can be continuously transformed into each other, for example, through the Bain's path [47]. The corresponding deformation and the evolution of the g_3 pattern is presented in Sect. II C 1.

Although bcc and fcc are easily distinguishable, it is certainly difficult to detect a small average excursion from either structure onto the Bain's path from a local structure analysis when thermal fluctuations are present. Tiny reductions of symmetry cannot be detected from a local analysis, e.g., in the immediate vicinity of a second-order phase transformation. A rigorous structure determination would necessitate a finite-size scaling analysis [48, 49].

The question arises how far the symmetry reduction must have proceeded in order to be visible in a g_3 analysis and if "typical" symmetry reductions can be detected. Two such examples are presented in Fig. 2: first, the A6 structure, which can be obtained from fcc through a deformation of the fcc unit cell; second, the A7 structure, which can be reached from simple cubic through a Peierls deformation [50], in which not only the shape of the unit cell but also the relative atomic positions change continuously. In both cases, certain peaks appear elongated and less symmetric in the deformed structure than in the high-symmetry structure.

The A6 structure of In at room temperature is strained by 7.5% in one [100] direction relative to fcc. This leads to noticeably elongated nearest-neighbor peaks in A6. The first clear qualitative difference between A6 and fcc in this case study occurs in the fourth-neighbor-shell near $r/d_{nn} = 2$, where the $\cos\theta = \pm 0.5$ peaks break up into

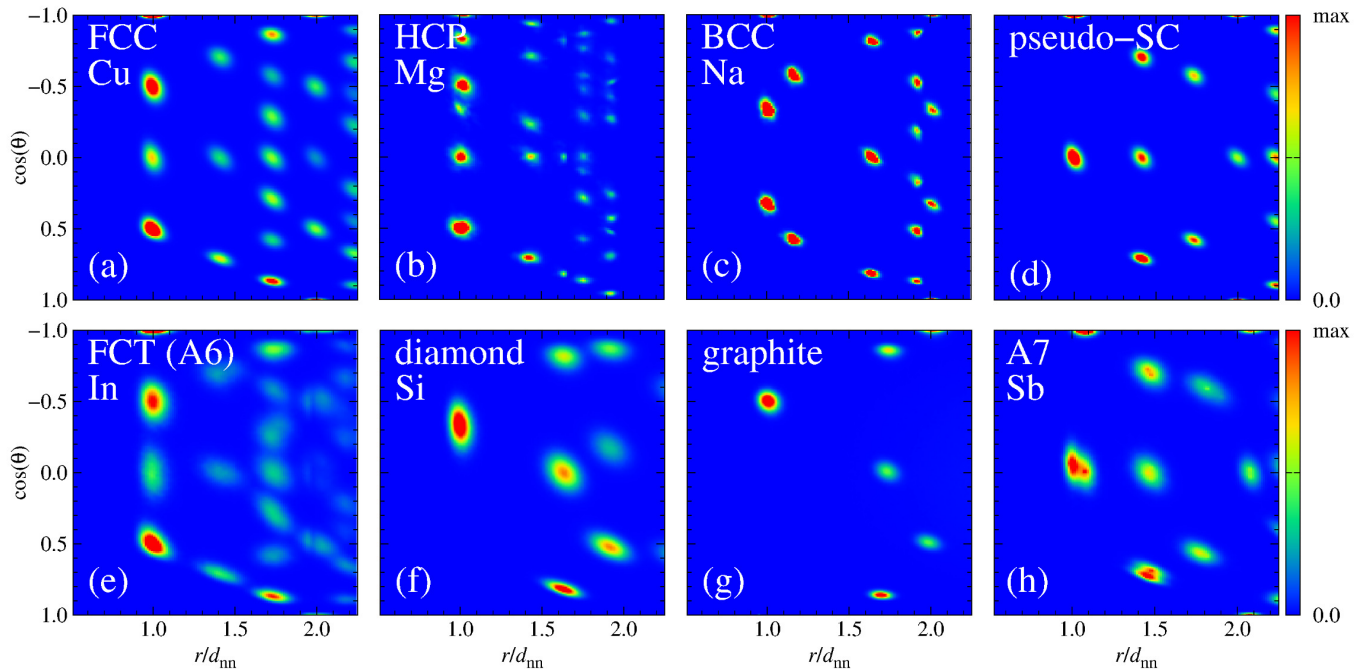


FIG. 2. $g_3(r, \theta)$ for the structures discussed in Sect. II C. The sequence of sub-figures is not consistent with the text, as to facilitate comparisons, e.g., between fcc and A6. Distances are normalized to nearest-neighbor spacings. In sub-figure (d), all atoms in NaCl were treated as being identical in the g_3 -analysis. This produces g_3 that is visually indistinguishable from that of a single-cubic (sc) structure – hence the name pseudo-sc. The corresponding RDFs are shown in Fig. S2.

two peaks. In contrast, the corresponding radial distribution function (not shown explicitly, see supplementary information for $g(r)$ figures.) has no obviously broken up peaks for the shown distances. In the case of the fourth-neighbor peak, this is because the contributions from $\cos \theta = \pm 1$ conceal the relative minimum in the radial distribution functions that are visible under $\cos \theta = \pm 0.5$, see Fig. 2(e). One might argue that effects can be deduced indirectly also from the RDF by fitting the various peaks of $g_2(r)$ with an appropriate sum over Gaussians. However, the significance of such fits would be small as the individual peaks are not necessarily Gaussian themselves. An asymmetric broadening of the peaks induced by thermal fluctuations could be falsely attributed to be caused by a (collective) displacive mode. For similar reasons, the distortion from fcc to A6 cannot be deduced from a (nearest-neighbor) bond-angle histogram $\text{Pr}(\theta)$ either. The skewness of the peaks in $\text{Pr}(\theta)$ is already non-negligible in the fcc phase. Thus, we would argue to have identified the first case, where a visual inspection of g_3 provides clearer evidence for the classification of symmetry from local analysis than a numerical post-analysis of the more common g_2 and nearest-neighbor bond-angle distribution function (BADF).

We next turn to the comparison between simple cubic and the A7 structure. Due to the Peierls distortion, the g_3 nearest-neighbor peak at $\cos \theta = 0$ develops a satellite along the radial direction, which reveals a deviation from local cubic symmetry as can be seen in Fig. 2(h). This

time, the analysis of g_2 would have detected a double peak as well. However, an added bonus of the g_3 analysis is that long bonds can be detected at 90° , as revealed by the satellites, as well as at 180° (since the center of mass of the $\theta = 180^\circ$ peak is located above the satellite rather than above the main $\theta = 90^\circ$ peak). In contrast, short bonds are located only near $\theta = 90^\circ$.

The last comparison of single-element, crystalline g_3 fingerprints relates to the diamond and the graphite lattices. This time, both the RDF and the BADF would also reveal a clear distinction between the two crystalline structures. However, it appears as if the clearest qualitative difference relates to the g_3 peak positions in the third neighbor shell, as can be seen by comparing Figs. 2(f) and (g). This difference might prove useful to discriminate clearly between different *in-silico* generated diamond-like carbon structures and to estimate the relative amount of domains in which carbon atoms bond through sp^2 and sp^3 hybridization.

1. Bain's path

In 1924, Bain suggested that bcc can transform continuously to fcc through a simple tetragonal deformation [47]: starting from bcc, the crystal is expanded in the [001] direction and contracted isotropically within the xy plane such that the deformation is volume conserving. This yields a body-centered tetragonal (bct) struc-

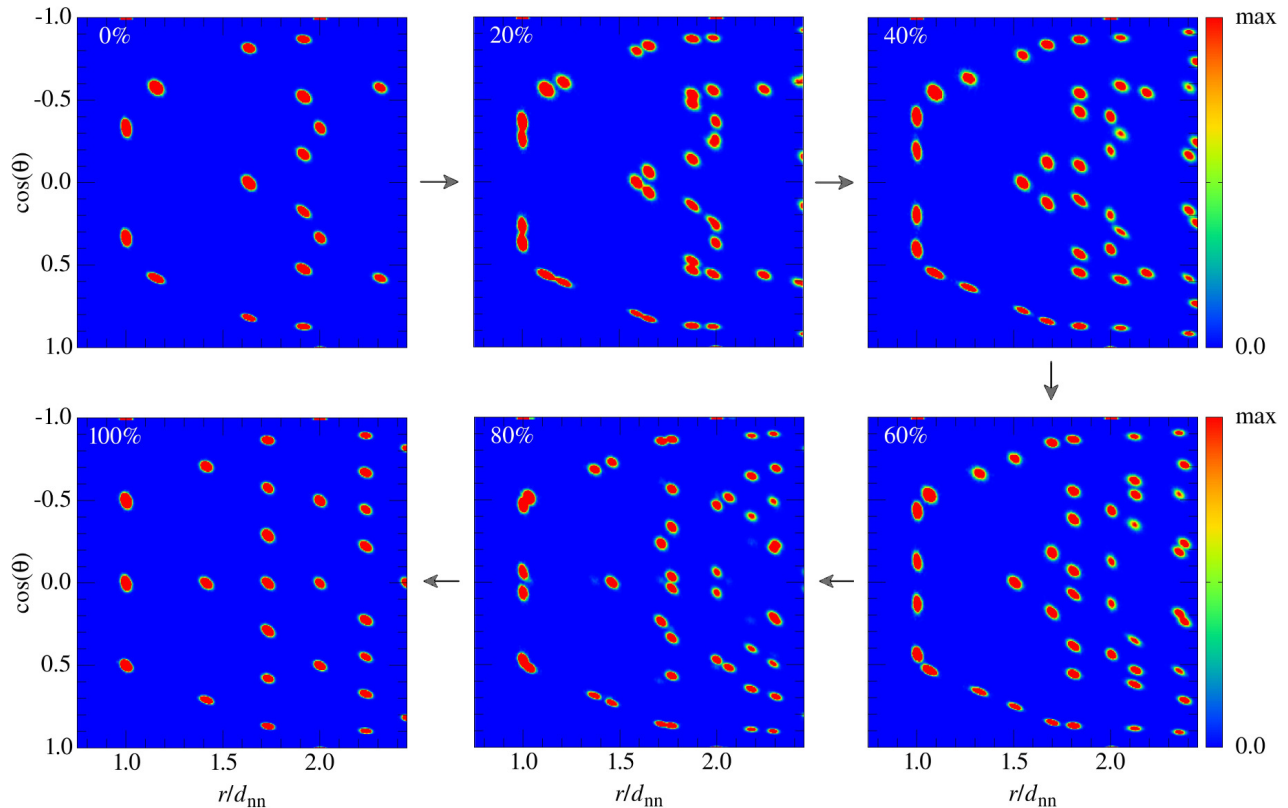


FIG. 3. $g(r, \theta)$ along the Bain’s path. The starting structure is bcc and the gradual deformation along the Bain’s path in percentages is given in the upper left corner of each graph. 0% corresponds to an ideal bcc structure, 100% - to an ideal fcc structure. The intermediate structures could be classified as bct. Distances are normalized to the pertinent nearest-neighbor spacing, which was estimated from the unit cell parameters. The corresponding RDFs are shown in Fig. S3.

ture between the two end-points of the Bain’s path. The density-conserving deformation to fcc is completed when the expansion in the [001] direction has reached a factor of $\sqrt[3]{2}$ and thus a factor of $\sqrt[6]{2}$ in the two orthogonal directions. While real phase transformations between bcc and fcc do not necessarily proceed along the Bain’s path but through paths yielding smaller activation energies, e.g., those proposed by Nishiyama-Wassermann [51, 52] and Kurdjumov-Sachs [53], we chose the Bain’s paths for reasons of simplicity.

Fig. 3 reveals how a continuous phase transformation driven by a lattice-distortive strain shows up in the proposed distribution function: initial peaks in $g(r, \theta)$ break up into two or sometimes three peaks. All peaks move as the strain increases and their majority merges with another peak in the final fcc structure. Along the Bain’s path, a familiar pattern is encountered: the A6 structure in Fig. 2(e) can be said to have progressed by approximately 92.5% along the Bain’s path and thus appears qualitatively most similar to the last configuration before the final fcc structure is reached.

III. APPLICATIONS

The local structure of liquids, amorphous solids, and other disordered condensed matter is often associated with that of crystals possessing long-range order. The latter are also termed “real solids” and set apart from glasses, which remain to be interpreted as highly viscous liquids. What may not always be clear, are the length scales—and also time scales—over which disordered condensed matter is indeed solid like. An important aspect of this section is to demonstrate that the analysis of g_3 provides quick and meaningful answers to this type of question.

The more general motivation for most applications considered in the following is again to explore strengths and weaknesses of a g_3 analysis. The section is organized such that the complexity—in the sense of deviation from simple crystalline order—increases with each case studied.

A. Grain boundaries

Grain boundaries (GBs) are one of the most elemental, two-dimensional defects in solids. They crucially effect

plasticity as well as electrical and thus thermal conductivity of metals. While they are rather straightforward to detect, to visualize, and to analyze [54], we wish to explore to what extent a g_3 analysis is able to reveal their presence as well. A low- Σ GB is considered with a rather weak perturbation of perfect crystallinity, thereby providing a challenging benchmark for our analysis.

Specifically, we consider a pair of $\Sigma 5$ -grain boundaries between two (001) surfaces in aluminium. The dimension of the GB is $4.0 \times 3.8 \text{ nm}^2$ within the GB planes and 2.8 nm in the direction normal to them. Periodic boundary conditions are applied in all three spatial directions. The GB is in the xy -plane of the simulation box. The number of repeat units in both crystallites having (001) surface is $n = 10$ yielding a relative number of atoms being directly part of the GB pair of 10%. The system is kept at a temperature of $T = 200 \text{ K}$ and a pressure of $p = 100 \text{ kPa}$. A snapshot of the simulation cell and of the GB geometry is shown in Fig. S1.

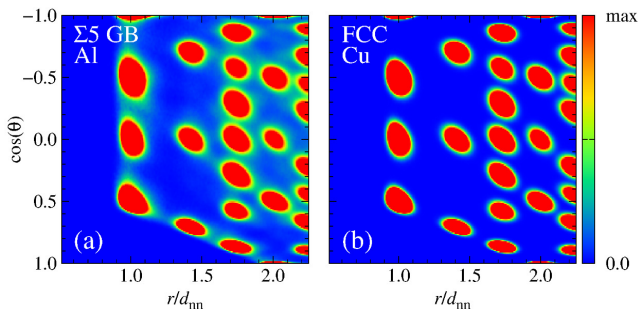


FIG. 4. $g(r, \theta)$ of (a) Al crystal with $\Sigma 5$ grain boundary at $T = 200 \text{ K}$, and of (b) Cu crystal at $T = 300 \text{ K}$. Distances are normalized to the pertinent nearest-neighbor spacing, which was estimated from the RDFs. The corresponding RDFs are shown in Fig. S4.

Fig. 4 shows the result for g_3 of the aluminium GB at 200 K and compares it to the 300 K data on fcc copper, which was already presented in Fig. 2(a). Since the number of atoms being part of the GB is relatively small, the focus in the g_3 analysis must be laid on the tails of the peaks, which is why the same data looks dramatically different in Fig. 2(a) and Fig. 4(b). At this point, it may be in place to remind the reader of the last paragraph in Sect. II A 1.

The presence of the investigated GB is only revealed by a rather small deformation of the peaks and by weak halos located exclusively around and between existing g_2 maxima, i.e., no significant structural compromises need to be made in the investigated GB. This observation is consistent with the low defect energy associated with the studied low- Σ grain boundaries. It remains to be seen to what extent a g_3 analysis allows one to estimate statistics on GBs.

B. Equilibrium liquids

1. Two simple, mono-atomic liquids

We now draw our attention to systems lacking long-range order and consider two simple, mono-atomic liquids first, namely argon and copper. We omit mentioning our motivation for studying these systems for reasons of brevity and hope that it becomes clear as the results are discussed.

Argon is modeled with a regular Lennard-Jones (LJ) potential, $V(r) = 4\epsilon\{(\sigma/r)^{12} - (\sigma/r)^6\}$, which is why we will sometimes refer to argon as to Lennard-Jones system in the following. Commonly used values for argon would be $\epsilon = 120 k_B K$ and $\sigma = 3.405 \text{ \AA}$, however, both values are set to unity in reduced units. In addition, we employ the frequently used LJ cut-off radius of $r_c = 2.5 \sigma$. A cubic simulation cell containing $N = 2000$ randomly placed atoms was set up at a fixed pressure of $p = 0.0024 \epsilon/\sigma^3$ and then equilibrated at a temperature of $T = 0.708 \epsilon/k_B$, which is just a few percent above the melting temperature and still below the boiling temperature. For these conditions, we found a relative packing fraction of $\eta_{\text{rel}} = 0.872$, which we define as the ratio of the liquid density and the density of a defect-free fcc crystal superheated to the liquid temperature.

The simulation of the copper melt encompasses $N = 4,000$ atoms. Atoms were initially placed on a diamond cubic lattice and equilibrated in a cubic simulation cell at a temperature of $T = 1,400 \text{ K}$ and a pressure of $p = 0.1 \text{ MPa}$. This makes the system be roughly 3% above the melting temperature at that pressure. For copper, the first estimate for the relative packing density of $\eta_{\text{rel}} = 0.940$ is deduced relative to that of a defect-free crystal superheated to 1,400 K. This estimate will be improved further below.

Figs. 5(a) and (c) convey quite similar bond-length, bond-angle correlations for copper and Lennard-Jones melt, where in both cases temperature was kept just a few percent above the melting temperature. In both cases, significant intensity is only found at the first-neighbor-shell distance, while relatively little (or smeared out) intensity exists at distances that would correspond to the second-nearest-neighbor distance in fcc or hcp. Interestingly, both liquids have a narrowing of intensity at the 90° bond angle in the nearest-neighbor shell, where both fcc and hcp have a maximum. It is therefore not meaningful to rationalize the liquid structure of Ar and Cu as having a close-packed structure resembling that of a crystal.

The view of a hard-sphere close random packing [55] appears much more appropriate for both Lennard-Jones system and copper than that of local crystalline order. In fact, both systems have the second peak in the RDF at about 1.8 times the typical bond-length distance, as can be deduced also indirectly from projecting intensities of the g_3 intensity onto the r/d_{nn} axis, which is typical for hard-sphere random packing. Moreover, the LJ

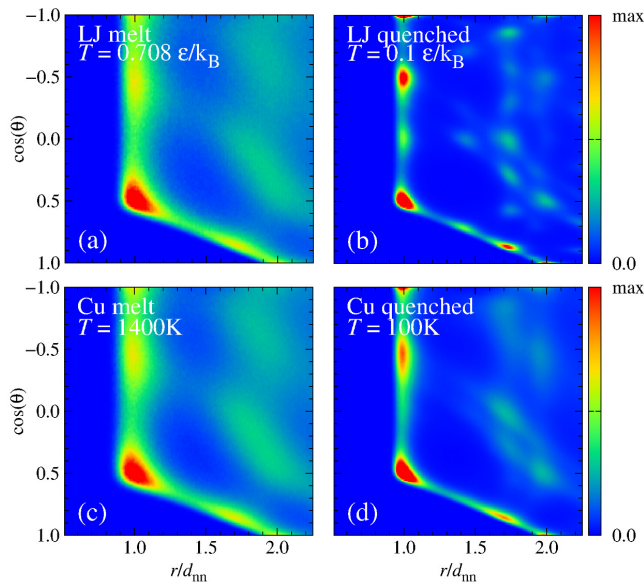


FIG. 5. $g_3(r, \theta)$ for a Lennard-Jones system at (a) $k_B T = 0.708\epsilon$ in thermal equilibrium and (b) quenched to $k_B T = 0.1\epsilon$ as well as for copper at (c) $T = 1400$ K and (d) quenched to $T = 100$ K. The corresponding RDFs are shown in Fig. S5.

system has a relative packing fraction close to estimates for random hard-sphere packing of $\eta_{\text{rhs}} \approx 0.855 \pm 0.01$, precise numbers being somewhat ill defined [56]. The value for copper deviates more clearly from that estimate. However, it has to be kept in mind that many-body interactions can lead to either bond-length contractions or extensions compared to that of crystalline reference structures, depending on whether an atom’s coordination number Z is decreased or increased. One could define an effective value for coordination number, Z_{eff} , in liquid copper through the (mean) charge density provided by the first-neighbor peak in $g(r)$ in units of the charge density of a single atom located a distance d_{NN} away from a central atom. This would yield a value of $Z_{\text{eff}} = 12.4$. Comparison of this value to the zero-moment of the first-neighbor peak of $Z = 11.7$, leads to an expected expansion of the bond length of about 2.3%, since the equilibrium bond length (in an ideal crystal structure) is proportional in the leading order to $\ln Z$ (see Eq. (31) and Fig. 1 in Ref. [30]). In turn, this yields a density increase of 7.3% and a modified estimate of $\eta_{\text{rhs}} = 0.876$, consistent with a dense, random hard-sphere packing for copper.

Despite the random-sphere packing analogy, the close similarity in the g_3 ’s between the LJ system and copper may remain somewhat surprising in light of the LJ potential being a two-body potential, for which the binding energy E_0 of ideal crystalline structures is roughly linear in Z , while the Gupta potential is a many-body potential for which E_0 scales approximately with $Z^{0.4}$. Thus, by simple rescaling of the Lennard-Jones coefficients, one would be in a position to reproduce a g_3 -measurement of

Cu reasonably well. Yet, the such-constructed potential would make awful predictions on a variety of material parameters, which crucially affect the material’s properties. In particular, defect energies (measured in units of the cohesive energy per atom) and ratios formed by the independent elastic tensor elements differ strongly between metals and any two-body potential [57], see also the large discrepancies of the ratio $\eta_{\text{mb}} = T_{\text{m}}/T_{\text{b}}$ for noble gases (LJ) and copper, or other metals, which are well described by the Gupta (G) potential, where $\eta_{\text{mb}}(\text{LJ})$ barely exceeds unity, while $\eta_{\text{mb}}(\text{G})$ is almost a factor of three. Thus, reproducing g_3 — and even more so reproducing the RDF — at a single state point should never be used as strong evidence for the accuracy of a potential.

Quenching the systems down to small temperatures appears to arrest the random packing structure to a significant degree. Signs of peaks at $\theta = 90^\circ$ are at best subtle for copper and somewhat more easily to ascertain in the case of a LJ system. Statistically speaking there appears to be a 60° symmetry axis but still very little intensity at distances where hcp and fcc have their nearest-neighbor shell. The marginal intensities in the second shell of LJ appear at the locations, where fcc but not hcp has peaks. Assessing to what degree the differences between the g_3 patterns in Cu and LJ system arise due to differences in (i) interaction potentials, (ii) packing densities or meaningfully undimensionalized (ii) cooling rates, and (iii) temperatures is beyond the scope of this work.

2. A Peierls-distorted liquid

While rare-gas atoms (LJ system) and simple metals (that is those that can be modeled with a Gupta or related embedding potentials) have no significantly directed interactions—in the sense of necessitating explicit angle or directional dependencies in the construction of transferable potentials—other elements do, in particular those that do not adopt close-packed structure in their elemental crystalline phase at small temperature and pressure. One such example is the metalloid antimony whose thermodynamically stable structure at ambient conditions is the rhombohedral A7 structure, which can be interpreted as a Peierls-distorted simple-cubic crystal, as already discussed in Sect. II C. Here, we investigate to what extent a g_3 -based analysis allows remnants of a Peierls deformation in the liquid phase to be more easily identified than with ordinary bond-angle distribution functions. Ref. [58] presents pertinent histograms for different cut-off radii are presented and discusses how a Peierls deformation in our system of interest may occur in the absence of long-range order.

To model liquid antimony, we use a cubic elementary cell with a particle number that is incompatible with a defect-free, simple-cubic or A7 structure, i.e., $N = \text{int}(5.5^3) = 166$ atoms. The initial structure was diamond with randomly drawn vacancies, as to prevent

the system from being locked into a superheated potentially Peierls-distorted simple-cubic solid. The system was thermostat at constant (experimental) density for 3 ps at $T = 1,100$ K, which is 20% above the melting temperature, and then equilibrated for another 3 ps at constant pressure. This was followed by two subsequent 2.5 ps runs, over which g_3 was accumulated. An additional, similar run was performed with $N = 200$ atoms, which also contained two 2.5 ps measurements. Since all measurements had no obvious differences other than random scatter, the results for g_3 were averaged to yield the data shown in Fig. 6.

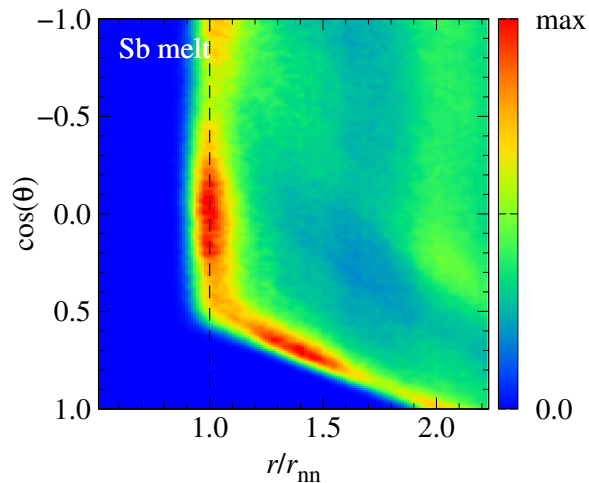


FIG. 6. $g_3(r, \theta)$ for liquid Sb at $T = 1100$ K. Distances are normalized to the pertinent nearest-neighbor spacing, which was estimated from the analysis of RDF of the melt. The corresponding RDFs are shown in Fig. S6.

In many aspects, Fig. 6 reveals a compromise between random-sphere packing and either a simple cubic or an A7 structure. The following features are indicative of the latter: The nearest-neighbor peak has increased intensity at 90° bond angles, as to be expected from atoms that form bonds with a valent, half-filled p -shell and a full outer s -shell. The increased intensity for the nearest-neighbor shell at 180° is shifted to slightly larger radii than those at 90° , whereby a local Peierls distortion is revealed. Moreover, the peak associated with the secondary bond angle of 45° is still visible, although it is smeared out substantially. However, other secondary or even tertiary peaks are no longer visible. Instead, increased intensity shows up at $r/d_{nn} \approx 2$ at $\cos \theta \lesssim 0.5$ as is the case for the random-sphere packing. However, this increased intensity lies at $r/d_{nn} < 2$ for random-sphere packing but at $r/d_{nn} > 2$ in liquid antimony. Another difference between the random (sphere) packing in liquid copper and that in liquid antimony is the absence of a significantly enhanced intensity at $\cos \theta = \pm 0.5$ in liquid antimony.

C. Out-of-equilibrium systems

The last case study presented in this work evolves around polyamorphism and the detection of coexisting disordered phases in a computer simulation. Polyamorphism refers to the existence of two distinct, disordered equilibrium phases, that is liquids, which are separated by a discontinuous phase transition. The possibility of polyamorphism was discussed controversially in the literature [59–61], because, in contrast to crystals, liquids were thought to evolve continuously as a function of pressure, temperature, or other intrinsic thermodynamic variables. In fact, we must admit that we managed to identify only a single, convincing work [59] reporting a first-order *equilibrium* (rather than supercooled) phase transition between two condensed phases both of which lacking any type of long-range order. The concept of polyamorphism is typically extended to and investigated in out-of-equilibrium disordered systems, i.e., glasses [62–65], although it often remains unclear if a certain anomaly in the response function of a glass can rightfully be associated with an underlying polymorphic phase transitions (PPT) of an equilibrium reference liquid.

Silicon is one of few materials for which the existence of a PPT in the supercooled and thus out-of-equilibrium liquid has been properly established [66, 67]. The reversible transformation between the two involved phases, namely, low-density, amorphous silicon (LDA-Si) and high-density, amorphous silicon (HDA-Si) occurs near 14 GPa upon compression and at 4 GPa under decompression. The local structure of LDA-Si has been found to resemble that of the cubic diamond structure (Si-I) with four nearest neighbors, while HDA-Si locally resembles β -tin (Si-II) with six nearest neighbors. Due to their structures, Si-I and likewise LDA-Si are semiconducting, while Si-II and HDA-Si are metallic [66, 67]. A question that arises is whether a g_3 -based analysis can clearly discriminate between the two structures, and, more importantly, identify their coexistence if applicable.

To produce different amorphous silicon structures, we proceeded as follows: A supercell of crystalline diamond silicon containing 1,728 atoms was equilibrated at a temperature of $T = 5,000$ K and atmospheric pressure. The sample was quenched at ambient pressure to $T = 1,000$ K, which is well below silicon’s melting point of $T_m \approx 1,700$ K. The $T = 1,000$ K sample is therefore deep in the glass phase. Thermal fluctuations are still large enough to smear out the nearest-neighbor g_3 peaks in the crystalline reference phase to a substantial amount as can be seen in Fig. 2(f) and again in Fig. 7(a), where the same data is shown.

In the next step, the sample was quenched down to room temperature and the applied pressure was increased with a ramp of 0.1 GPa/ps. Just before 15 GPa was reached, the density suddenly increased, which is indicative of a pressure-driven PPT from the LDA to the HDA silicon phase. The transition pressure is close to the value

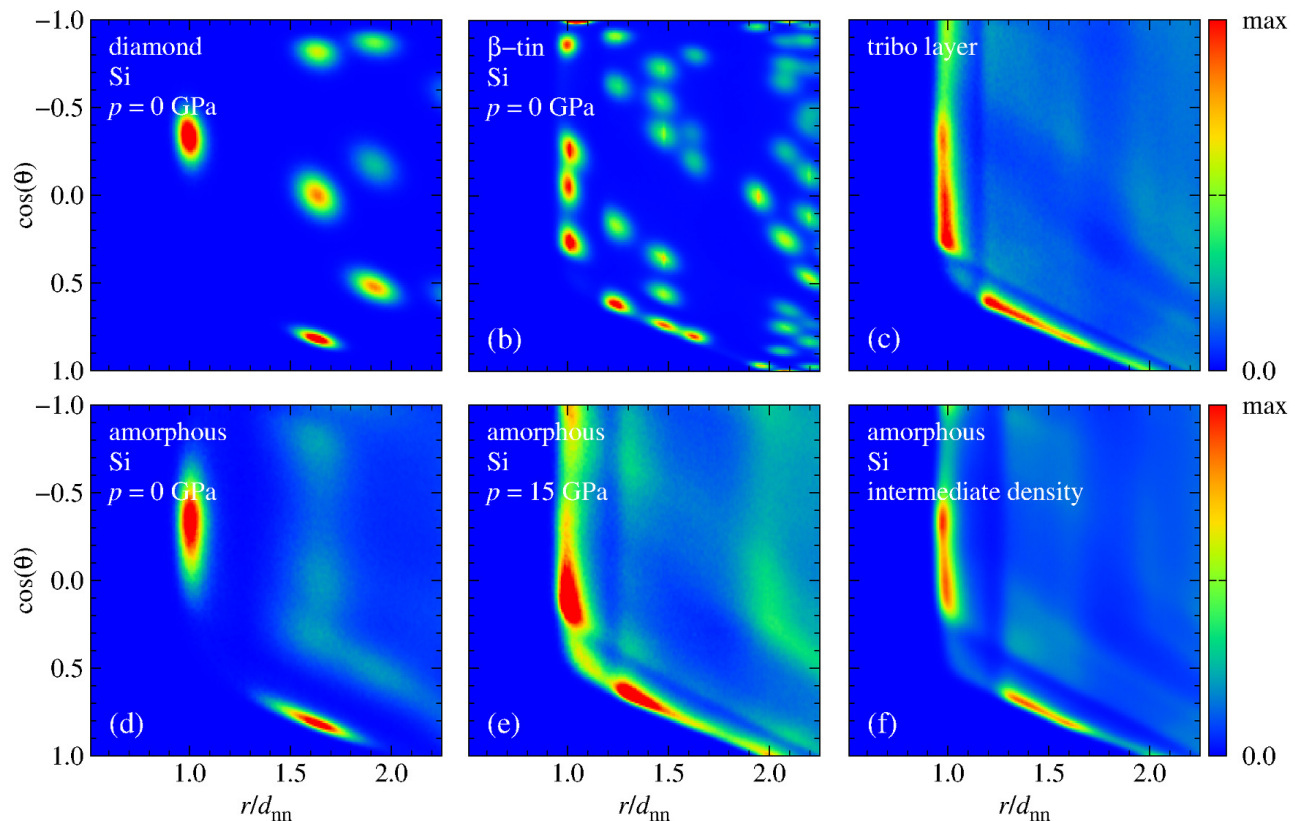


FIG. 7. $g(r, \theta)$ for (a) diamond Si structure, (b) β -tin structure of Si, (c) the amorphous Si obtained in a sliding experiment of two diamond blocks at external pressure of $p = 11$ GPa (see text for more details), (d) amorphous Si at pressure $p = 0$ GPa, (e) amorphous Si at pressure $p = 15$ GPa, and (f) amorphous Si equilibrated at intermediate density (see text for more details). Distances are normalized to the pertinent nearest-neighbor spacing, which was estimated from the analysis of RDF of the melt. The corresponding RDFs are shown in Fig. S7.

of 14 GPa reported in Ref. [42]. Upon further compression to 25 GPa, additional quasi-discontinuities occurred neither in volume nor in energy. A configuration with a density half way between the LDA and the HDA density was kept and further equilibrated at 300 K at fixed volume.

Representative g_3 functions occurring during the just-described thermo-mechanical protocol are depicted in Fig. 7(d)–(f). The LDA silicon phase reveals predominantly nearest-neighbor bond angles close to the tetrahedral bond angle for which $\cos \theta = -1/3$. At larger distances, no ternary bond-angle peaks are noticeable, which means that a diamond-like domain extends over less than two nearest-neighbor spacings. The HDA silicon phase has increased intensity in the nearest-neighbor shell near and predominantly just below $\theta = 90^\circ$ as well as just below $\theta = 180^\circ$. Remnants of the β -tin, next-nearest-neighbor shell, see Fig. 7(b), are also present in HDA silicon but increased intensity is absent with regard to ternary angles. Thus, our analysis corroborates the finding that local order in LDA and HDA silicon is similar to that found in the diamond and the β -tin structure, respectively. In addition, we find that not only positional but also orientational order is short ranged and does not

extend past distances exceeding twice the bond length.

Note that g_3 of LDA-Si equilibrated for longer times at around $p = 8$ GPa develops nearest-neighbor peaks, which are elongated with significant intensity along the $\cos \theta$ -axis all the way to slightly negative values (not shown explicitly). From this observation, it can be concluded that the tetrahedrally coordinated Si atom in the two considered amorphous samples experience a local pressure of less than 8 GPa.

For intermediate densities, Fig. 7(f) reveals coexistence of LDA and HDA through the presence of two pertinent peaks in the nearest-neighbor shell having similar intensity. Coexistence could have been also easily deduced from a regular bond-angle histogram, in particular because the first two neighbor shells are well separated. The added insight of our analysis is that local order can be said to not extent in any statistically relevant way beyond the second neighbor shell.

As the last application of this study, we analyze the atomistic structure of a tribological layer, which Moras *et al.* [42] produced in the force-field based simulation of an unlubricated contact between two Si-I, single crystals under the combined action of normal compression and lateral sliding. They found interfacial shear-assisted

amorphization at room temperature. An interesting observation in this work was that the density in the tribo layer was already relatively close to that of β -tin even when normal stresses were still well below the hydrostatic PPT pressure of 14 GPa. By analyzing radial and angular distribution function, they found the tribo-introduced layer to resemble predominantly HDA silicon.

To further analyze the structure in the silicon tribo layer, we calculated the mixed radial-angular distribution function of the amorphous region, which had been obtained after 15 ns sliding at a 10 m/s velocity and an applied external normal pressure of $p = 11$ GPa. Our result shown in Fig. 7(c) confirms the conclusion of a mixed Si-I and Si-II local structure through the increased primary peak intensity at $\cos\theta \approx -0.3$ and slightly positive $\cos\theta$ values, respectively. One difference between the system that we produced at intermediate density and the tribo layer of Moras *et al.* is that the tribo layer has a slightly larger relative weight on the Si-II phase. Moreover, the primary g_3 peaks are broader and more asymmetric in the tribo layer. This can be easily attributed to the stress being anisotropic within the amorphous tribo layer, which should lead to a distortion of crystalline reference structures. The distortion of peaks should be particularly large when the shear modulus is small, which would explain why the peak associated with the β -tin-like structure is more asymmetric than the one belonging to tetrahedral local order. In addition, we find that local order is similarly short ranged in the tribo layer as in the amorphous structures obtained via the cooling/compression protocol under hydrostatic pressure.

For both amorphous silicon samples, we tested (visually) to what extent the phase separation of HDA and LDA silicon is indeed local. This was done by labeling and representing atoms as high-, low-, or intermediate density, depending on the size of their Voronoi cell. Atoms were said to belong to a high- (low-) density domain, if their Voronoi volume was less than 98% (more than 102%) of the mean volume per atom. Roughly one third fell into either category for both samples with a slightly larger weight (40%) on the high-density atoms in the tribo layer and (38%) in the intermediate-density sample. No larger clusters were discernible to the naked eye when looking at such produced configuration files, which is consistent with the finding from the g_3 analysis that structural correlations are short ranged.

IV. CONCLUSIONS

In this work, we proposed a mixed radial, orientational distribution function for the analysis of local order and applied it to various elemental condensed-matter systems. The central beneficial property of the correlation function is that it allows local and intermediate-scale angular correlations to be deduced simultaneously with little effort in a single graph. For example, the structure of liquid copper and LJ melt can be readily associ-

ated with random-sphere packing, while the aluminium grain boundary, which effectively represents a nanocrystalline material, leads to graphs of the correlation function, which are difficult to distinguish from that of a perfect crystal. In fact, detailed features of angular correlations are clearly visible even in the fifth coordination shell for the given nanocrystalline material, while orientational correlations for random-sphere packing are rather minor beyond the nearest-neighbor shell. At the same time, the tails of the correlation function for nanocrystalline aluminium contains features, i.e., smeared-out intensity around individual peaks, which clearly point to the presence of lattice defects.

Although the proposed correlation function is local and thus intrinsically unable to detect rigorously subtle structural change occurring as collective phenomena, we presented a few examples, for which signs of such changes could be detected. These were small-amplitude symmetry reductions of a unit cell including minor excursions on the Bain's path connecting fcc and bcc as well as a Peierls distortion from simple cubic to rhombohedral A7.

Of course, the proposed analysis also has shortcomings. The introduced correlation function is not necessarily sensitive to every (collective) mode or every local symmetry. One such example, which we plan on discussing in a forth-coming work, appears to be the rigid-unit modes turning β into α quartz. In addition, the correlation function cannot discriminate (without further quantitative analysis) between certain structural motifs, in particular when they have the same (relative amount) of bond angles, at least not when considering only intensity in the first neighbor shell. As an example, imagine the local binding in octahedral, square-pyramidal, and seesaw geometries. All structural motifs have equilibrium bond angles at or near 90° and 180° and they have same relative amount, namely 2:1. While a quantitative processing would allow pure octahedral or pure seesaw geometry to be determined, it would not be possible, based on a combined $g(r)$ and $g_3(r, \theta)$ analysis alone, to discriminate between pure square-pyramidal and mixed octahedral/seesaw local orders. The final limitation discussed in this section is that deducing order parameters from the correlation function would necessitate further considerations of how precisely a bond is labeled or weighted as a nearest-neighbor bond.

Despite the just-mentioned shortcomings, the potentially most interesting application of the proposed correlation function is the possibility to detect coexistence of competing phases in disordered systems. Our analysis revealed with little effort that two different forms of high-pressure amorphous silicon—one being obtained traditionally through quenching a melt and application of hydrostatic pressure, the other one through the tribo-induced amorphization of a crystal at room temperature—has coexisting diamond-like and β -tin like domains. The size of these domains was easily determined to be extremely small for both classes without performing further analysis. In our forthcoming work,

we plan on demonstrating that the controversial discussion [3, 61, 68] on whether liquid silica (as described by the potential of van Beest, Kramers, and van Santen [69]) contains coexisting “liquid quartz” and “liquid cristobolite” would have come to a quick, conclusive end, if simulators had only made use of the proposed correlation function.

For the future, we hope that applications can be identified in which the mixed radial, angular correlation function proves useful to provide *initial* answers to scientific problems rather than clearer versions of answers that are already known. To assist others in achieving this, we uploaded our analysis code to the supplementary materials section.

V. DATA AVAILABILITY

The data that support the findings of this study are available from the corresponding author upon reasonable

request.

VI. SUPPLEMENTARY INFORMATION

See supplementary information for radial distribution functions of all systems discussed in this article. The C++ code for calculation of the described three-body correlation function is also attached to the supplementary information.

-
- [1] P. H. Poole, F. Sciortino, T. Grande, H. E. Stanley, and C. A. Angell, *Physical Review Letters* **73**, 1632 (1994), URL <https://doi.org/10.1103/physrevlett.73.1632>.
- [2] E. A. Jagla, *Journal of Physics: Condensed Matter* **11**, 10251 (1999), URL <http://stacks.iop.org/0953-8984/11/i=50/a=317>.
- [3] I. Saika-Voivod, P. H. Poole, and F. Sciortino, *Nature* **412**, 514 (2001), URL <https://doi.org/10.1038/2F35087524>.
- [4] N. B. Wilding and J. E. Magee, *Physical Review E* **66** (2002), URL <https://doi.org/10.1103/physreve.66.031509>.
- [5] L. Liu, S.-H. Chen, A. Faraone, C.-W. Yen, and C.-Y. Mou, *Physical Review Letters* **95** (2005), URL <https://doi.org/10.1103/physrevlett.95.117802>.
- [6] K. Stokely, M. G. Mazza, H. E. Stanley, and G. Franzese, *Proceedings of the National Academy of Sciences* **107**, 1301 (2010), URL <https://doi.org/10.1073/pnas.0912756107>.
- [7] A. V. Kolobov, P. Fons, A. I. Frenkel, A. L. Ankudinov, J. Tominaga, and T. Uruga, *Nature Materials* **3**, 703 (2004), URL <https://doi.org/10.1038/nmat1215>.
- [8] D. Shakhvorostov, R. A. Nistor, L. Krusin-Elbaum, G. J. Martyna, D. M. News, B. G. Elmegreen, X. h. Liu, Z. E. Hughes, S. Paul, C. Cabral, et al., *Proceedings of the National Academy of Sciences* **106**, 10907 (2009), URL <https://doi.org/10.1073/pnas.0812942106>.
- [9] M. Allen and D. Tildesley, *Computer Simulation of Liquids* (Oxford: Clarendon Pr, 1987).
- [10] S. V. Sukhomlinov and M. H. Müser, *The Journal of Chemical Physics* **146**, 024506 (2017), URL <https://doi.org/10.1063/1.4973804>.
- [11] A. D. J. Haymet, S. A. Rice, and W. G. Madden, *The Journal of Chemical Physics* **74**, 3033 (1981), URL <https://doi.org/10.1063/1.441427>.
- [12] R. Z. Troitzsch, G. J. Martyna, S. E. McLain, A. K. Soper, and J. Crain, *The Journal of Physical Chemistry B* **111**, 8210 (2007), URL <https://doi.org/10.1021/jp0714973>.
- [13] O. M. Lutz, T. S. Hofer, B. R. Randolf, and B. M. Rode, *Chemical Physics Letters* **536**, 50 (2012), URL <https://doi.org/10.1016/j.cpllett.2012.03.065>.
- [14] J. A. Krumhansl and S. shion Wang, *The Journal of Chemical Physics* **56**, 2034 (1972), URL <https://doi.org/10.1063/1.1677495>.
- [15] W. J. McNeil, W. G. Madden, A. D. J. Haymet, and S. A. Rice, *The Journal of Chemical Physics* **78**, 388 (1983), URL <https://doi.org/10.1063/1.444514>.
- [16] G. Hummer and D. M. Soumpasis, *The Journal of Chemical Physics* **98**, 581 (1993), URL <https://doi.org/10.1063/1.464600>.
- [17] G. Hummer, A. E. García, and D. M. Soumpasis, *Faraday Discuss.* **103**, 175 (1996), URL <https://doi.org/10.1039/fd9960300175>.
- [18] A. E. García, G. Hummer, and D. M. Soumpasis, *Proteins: Structure, Function, and Genetics* **27**, 471 (1997), URL [https://doi.org/10.1002/\(sici\)1097-0134\(199704\)27:4<471::aid-prot1>3.0.co;2-e](https://doi.org/10.1002/(sici)1097-0134(199704)27:4<471::aid-prot1>3.0.co;2-e).
- [19] C. Peltz, A. Baranyai, A. A. Chialvo, and P. T. Cummings, *Molecular Simulation* **29**, 13 (2003), URL <https://doi.org/10.1080/0892702031000065692>.
- [20] D. Dhabal, M. Singh, K. T. Wikfeldt, and C. Chakravarty, *The Journal of Chemical Physics* **141**, 174504 (2014), URL <https://doi.org/10.1063/1.4898755>.
- [21] D. Dhabal, K. T. Wikfeldt, L. B. Skinner, C. Chakravarty, and H. K. Kashyap, *Physical Chemistry Chemical Physics* **19**, 3265 (2017), URL <https://doi.org/10.1039/c6cp07599a>.
- [22] M. Singh, D. Dhabal, A. H. Nguyen, V. Molinero, and C. Chakravarty, *Physical Review Letters* **112** (2014), URL <https://doi.org/10.1103/physrevlett>.

- 112.147801.
- [23] D. Dhabal, A. H. Nguyen, M. Singh, P. Khatua, V. Molinero, S. Bandyopadhyay, and C. Chakravarty, *The Journal of Chemical Physics* **143**, 164512 (2015), URL <https://doi.org/10.1063/1.4933420>.
- [24] P. J. Steinhardt, D. R. Nelson, and M. Ronchetti, *Physical Review B* **28**, 784 (1983), URL <https://doi.org/10.1103/physrevb.28.784>.
- [25] W. Mickel, S. C. Kapfer, G. E. Schröder-Turk, and K. Mecke, *The Journal of Chemical Physics* **138**, 044501 (2013), URL <https://doi.org/10.1063/1.4774084>.
- [26] C. Quintale and L. Degrève, *Journal of Molecular Structure: THEOCHEM* **282**, 159 (1993), URL [https://doi.org/10.1016/0166-1280\(93\)85046-2](https://doi.org/10.1016/0166-1280(93)85046-2).
- [27] L. Degrève and C. Quintale, *Electrochimica Acta* **38**, 1405 (1993), URL [https://doi.org/10.1016/0013-4686\(93\)80077-d](https://doi.org/10.1016/0013-4686(93)80077-d).
- [28] J.-W. Shen, O. Kitao, and K. Nakanishi, *Fluid Phase Equilibria* **120**, 81 (1996), URL [https://doi.org/10.1016/0378-3812\(96\)02996-2](https://doi.org/10.1016/0378-3812(96)02996-2).
- [29] R. P. Gupta, *Physical Review B* **23**, 6265 (1981), URL <https://doi.org/10.1103/physrevb.23.6265>.
- [30] J. Jalkanen and M. H. Müser, *Modelling and Simulation in Materials Science and Engineering* **23**, 074001 (2015), URL <http://dx.doi.org/10.1088/0965-0393/23/7/074001>.
- [31] J. P. Perdew, M. Ernzerhof, and K. Burke, *The Journal of Chemical Physics* **105**, 9982 (1996), URL <https://doi.org/10.1063/1.472933>.
- [32] G. Lippert, J. Hutter, and M. Parrinello, *Molecular Physics* **92**, 477 (1997), URL <https://doi.org/10.1080/002689797170220>.
- [33] J. Hutter, M. Iannuzzi, F. Schiffmann, and J. VandeVondele, *Wiley Interdisciplinary Reviews: Computational Molecular Science* **4**, 15 (2013), URL <https://doi.org/10.1002/wcms.1159>.
- [34] J. VandeVondele and J. Hutter, *The Journal of Chemical Physics* **127**, 114105 (2007), URL <https://doi.org/10.1063/1.2770708>.
- [35] S. Goedecker, M. Teter, and J. Hutter, *Physical Review B* **54**, 1703 (1996), URL <https://doi.org/10.1103/physrevb.54.1703>.
- [36] C. Hartwigsen, S. Goedecker, and J. Hutter, *Physical Review B* **58**, 3641 (1998), URL <https://doi.org/10.1103/physrevb.58.3641>.
- [37] X. Zhou, F. Doty, and P. Yang, *Computational Materials Science* **50**, 2470 (2011), URL <https://doi.org/10.1016/j.commatsci.2011.03.028>.
- [38] J. Tersoff, *Physical Review B* **39**, 5566 (1989), URL <https://doi.org/10.1103/physrevb.39.5566>.
- [39] T. Kumagai, S. Izumi, S. Hara, and S. Sakai, *Computational Materials Science* **39**, 457 (2007), URL <https://doi.org/10.1016/j.commatsci.2006.07.013>.
- [40] Y. Mishin, D. Farkas, M. J. Mehl, and D. A. Papaconstantopoulos, *Physical Review B* **59**, 3393 (1999), URL <https://doi.org/10.1103/physrevb.59.3393>.
- [41] S. Plimpton, *Journal of Computational Physics* **117**, 1 (1995), URL <http://dx.doi.org/10.1006/JCPH.1995.1039>.
- [42] G. Moras, A. Klemenz, T. Reichenbach, A. Gola, H. Uetsuka, M. Moseler, and L. Pastewka, *Physical Review Materials* **2** (2018), URL <https://doi.org/10.1103/physrevmaterials.2.083601>.
- [43] T. Schneider and E. Stoll, *Physical Review B* **17**, 1302 (1978), URL <https://doi.org/10.1103/physrevb.17.1302>.
- [44] G. Bussi, D. Donadio, and M. Parrinello, *The Journal of Chemical Physics* **126**, 014101 (2007), URL <https://doi.org/10.1063/1.2408420>.
- [45] G. J. Martyna, M. L. Klein, and M. Tuckerman, *The Journal of Chemical Physics* **97**, 2635 (1992), URL <https://doi.org/10.1063/1.463940>.
- [46] H. J. Beister, K. Strössner, and K. Syassen, *Physical Review B* **41**, 5535 (1990), URL <https://doi.org/10.1103/physrevb.41.5535>.
- [47] E. C. Bain and N. Y. Dunkirk, *Trans. AIME* **70**, 25 (1924).
- [48] M. S. S. Challa, D. P. Landau, and K. Binder, *Physical Review B* **34**, 1841 (1986), URL <https://doi.org/10.1103/physrevb.34.1841>.
- [49] K. Binder, *Reports on Progress in Physics* **50**, 783 (1987), URL <https://doi.org/10.1088/0034-4885/50/7/001>.
- [50] J.-P. Gaspard, A. Pellegatti, F. Marinelli, and C. Bichara, *Philosophical Magazine B* **77**, 727 (1998), URL <https://doi.org/10.1080/13642819808214831>.
- [51] Z. Nishiyama, *The Science reports of the Tôhoku Imperial University* **23**, 637 (1934).
- [52] G. Wassermann, *Archiv für das Eisenhüttenwesen* **16**, 647 (1933).
- [53] G. Kurdjumow and G. Sachs, *Zeitschrift für Physik* **64**, 325 (1930), URL <https://doi.org/10.1007/bf01397346>.
- [54] A. Stukowski, *Modelling and Simulation in Materials Science and Engineering* **18**, 015012 (2009), URL <https://doi.org/10.1088/0965-0393/18/1/015012>.
- [55] G. D. SCOTT, *Nature* **194**, 956 (1962), URL <https://doi.org/10.1038/194956a0>.
- [56] S. Torquato, T. M. Truskett, and P. G. Debenedetti, *Physical Review Letters* **84**, 2064 (2000), URL <https://doi.org/10.1103/physrevlett.84.2064>.
- [57] S. V. Sukhominov and M. H. Müser, *Journal of Physics: Condensed Matter* **28**, 395701 (2016), URL <https://doi.org/10.1088/0953-8984/28/39/395701>.
- [58] K. Seifert, J. Hafner, and G. Kresse, *J. Non-Cryst. Sol.* **207**, 871 (1996).
- [59] Y. Katayama, T. Mizutani, W. Utsumi, O. Shimomura, M. Yamakata, and K. ichi Funakoshi, *Nature* **403**, 170 (2000), URL <https://doi.org/10.1038/35003143>.
- [60] P. F. McMillan, G. N. Greaves, M. Wilson, M. C. Wilding, and D. Daisenberger, in *Liquid Polymorphism* (John Wiley & Sons, Inc., 2013), pp. 309–353, URL <https://doi.org/10.1002/9781118540350.ch12>.
- [61] E. Lascaris, M. Hemmati, S. V. Buldyrev, H. E. Stanley, and C. A. Angell, *The Journal of Chemical Physics* **140**, 224502 (2014), URL <https://doi.org/10.1063/1.4879057>.
- [62] E. Ponyatovsky and O. Barkalov, *Materials Science Reports* **8**, 147 (1992), URL [https://doi.org/10.1016/0920-2307\(92\)90007-n](https://doi.org/10.1016/0920-2307(92)90007-n).
- [63] P. H. Poole, T. Grande, C. A. Angell, and P. F. McMillan, *Science* **275**, 322 (1997), URL <https://doi.org/10.1126/science.275.5298.322>.
- [64] C. A. Angell, K. L. Ngai, G. B. McKenna, P. F. McMillan, and S. W. Martin, *Journal of Applied Physics* **88**, 3113 (2000), URL <https://doi.org/10.1063/1.1286035>.

- [65] J. L. Yarger, *Science* **306**, 820 (2004), URL <https://doi.org/10.1126/science.1104417>.
- [66] S. K. Deb, M. Wilding, M. Somayazulu, and P. F. McMillan, *Nature* **414**, 528 (2001), URL <https://doi.org/10.1038/35107036>.
- [67] P. F. McMillan, M. Wilson, D. Daisenberger, and D. Machon, *Nature Materials* **4**, 680 (2005), URL <https://doi.org/10.1038/nmat1458>.
- [68] P. H. Poole, M. Hemmati, and C. A. Angell, *Physical Review Letters* **79**, 2281 (1997), URL <https://doi.org/10.1103/physrevlett.79.2281>.
- [69] B. W. H. van Beest, G. J. Kramer, and R. A. van Santen, *Physical Review Letters* **64**, 1955 (1990), URL <https://doi.org/10.1103/physrevlett.64.1955>.